Exploration of Linear and Non-Linear Double Exposure Techniques by Simulation

John S. Petersen[a], Robert T. Greenway[a],
Tim Fühner[b], Peter Evanschitzky[b], Feng Shao[b] and Andreas Erdmann[b]

[a]Petersen Advanced Lithography, Inc.
12325 Hymeadow Dr. Suite 2-201 Austin, Texas 78750-1847, USA

[b]Fraunhofer Institute of Integrated Systems and Device Technology (IISB)
Schottkystrasse 10, 91058 Erlangen, Germany

ABSTRACT

In this work, a framework for the assessment of different double exposure techniques is laid out. Both the simulation environment and the utilized models, derived from well-established resist models, are discussed. Numerous simulation results are evaluated to investigate strengths and weaknesses of different double exposure approaches. Non-linear superposition techniques are examined in respect of their process performance for both standard and sub 0.25 k_1 values. In addition to a study of these effects in the scope of basic layouts, an application to interference-assisted lithography (IAL) is proposed and discussed.

Keywords: double exposure, double patterning, interference-assisted lithography, non-linear superposition, simulation study

1. INTRODUCTION

Comprehensive application of resolution enhancement techniques (RETs) such as off-axis illumination (OAI), optical proximity correction (OPC) and phase-shifting masks, is inevitable to print features with k_1 factors below 0.5. Despite the aggressive application of these techniques, for example, using recent computational lithography approaches like source/mask optimization, the process windows are reduced with increasingly smaller feature sizes and k_1 values. Moreover, only specific feature types and designs can be printed with a reasonable process window. For example, an interference of two coherent waves can be used to generate dense lines and spaces with a theoretically infinitely large depth of focus. The minimum pitch $p_{\min}$ of the dense line/space pattern is limited by the wavelength λ, the sine of the half angle α between the interfering waves and the refractive index n_i of the material in which the image is generated: $p_{\min} \leq \lambda/(2n_i \sin\alpha)$. This corresponds to a resolution limit for the half-pitch of 0.25 λ/NA or a minimum k_1 of 0.25. Semi-dense or isolated features, however, are not subject to such a stringent resolution limit. Such features can be printed with a considerably smaller k_1. In practice, the resolution limit of isolated and semi-dense features is limited by the size of the process window. Specific illuminator shapes and OPC of the mask features are used to increase process windows to largest possible sizes.

Double exposure and patterning help to relax these rigorous requirements by splitting a layout to two (or more) sub-sets which can be more easily printed. Subsequent exposure and processing of vertical and horizontal lines and spaces patterns can be used to create arrays of contact holes with superior lithographic performance.[1,2] A combination of interference exposures with appropriate trim exposures helps to fabricate regular design patterns.[3,4] Subsequent exposures of interlaced semi-dense lines in combination with optical non-linearities can be used to create dense lines/spaces with k_1 factors below 0.25.[5] Some of the mentioned splitting and exposure techniques can be realized by a straightforward linear superposition of two exposures, others require a non-linearity in the superposition of exposures (double exposures) or resist chemistries (litho-litho-etch [LLE] type double patterning processes). This paper explores the lithographic performance of different superposition options and corresponding double exposure and double patterning techniques by appropriate simulation techniques.

Further author information: John S. Petersen: Phone: (512) 241-1104, Fax: (512) 241-1105, jpetersen@advlitho.com
Andreas Erdmann: Phone: +49 (0)9131 761-258, Fax: +49 (0)9131 761-212, andreas.erdmann@iisb.fraunhofer.de

Highly accurate and efficient image simulation in combination with a flexible simulation infrastructure, which provides direct access to intermediate results and supports various superposition options, helps to explore many different splitting scenarios and superposition options. Section 2 introduces the new imaging kernel of the lithography simulator Dr.LiTHO, developed at the Fraunhofer IISB, which provides the required functionality and flexibility. Section 3 introduces several non-linear image superposition options and explores their advantages and challenges for basic configurations such as pitch division for dense lines and the formation of contact holes by a subsequent exposure of orthogonal line patterns. The application of the splitting and superposition to more complex layouts is demonstrated in Section 4. Specifically, the performance of interference-assisted lithography (IAL) in combination with various double exposure and double patterning options is studied.

2. A NEW ABBE IMAGING TOOL

In this work, numerous simulation experiments have been carried out. The feasibility of such a study strongly depends on the accuracy and efficiency of the employed simulator. Moreover, a high degree of flexibility, allowing for custom simulation flows, or access and user-defined manipulation of (intermediate) results, is indispensable. In this section, a new imaging tool that has been developed at IISB to meet these requirements is briefly discussed.

This new imaging tool, called *Dr.Image*, is based on a classical Abbe approach, however incorporating several extensions and improvements. Most importantly, the mask near field is accurately propagated through the imaging system by its fully vectorial representation. The vectorial pupil transfer function of the projection lens is computed only for occurring diffraction orders of the mask diffraction spectrum. Thus, the computation of an image for an individual source point does not involve any sampling. A sampling is only performed for the illumination source, since the Abbe formulation, used in this approach, depends on a finite number of source points: For each of these points an image is calculated. The incoherent superposition of all so obtained images then yields the total image. Defining an optimum source sampling that leads to a high accuracy while still maintaining a short computation time is a critical issue. This is solved in two ways: The user can either manually specify the source points, or a radial and tangential density for an automatic sampling distribution, which accounts for the geometry of the illumination source, can be defined. In the future, algorithms to identify ideal density settings will also be developed.

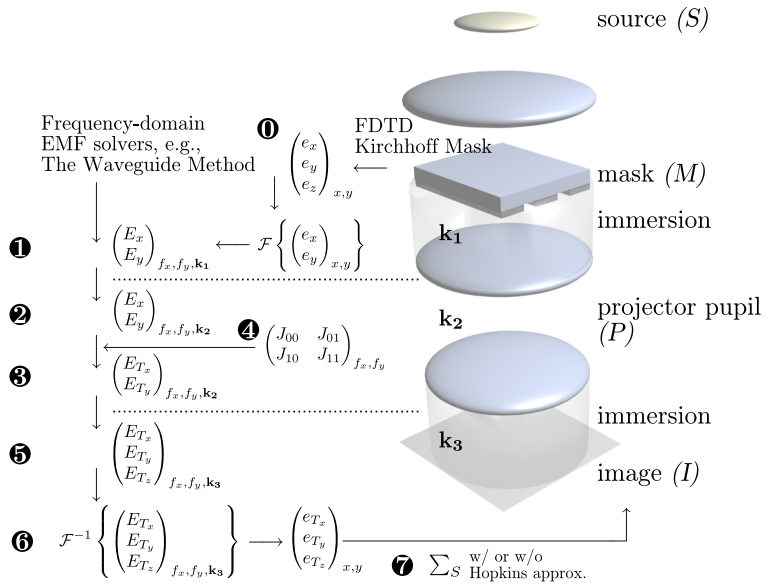

Figure 1. Schematic view of the new simulation model. The call-out numbers (0-7) correspond to the imaging process steps (see text for detailed description). $\mathbf{k_1}$ to $\mathbf{k_3}$ denote the k-factors at each light propagation region.

Figure 1 schematically demonstrates the simulation flow. As input, a Kirchhoff mask description or a mask diffraction spectrum has to be provided (0). In case of a thin mask, a simple Fourier transform leads to the

diffraction spectrum. Rigorous electro-magnetic-field (EMF) solvers can be used to obtain accurate diffraction spectra, that are often required in the scope of advanced lithographic projection systems. If the result of the applied solver is a field (e.g. Finite-Difference Time-Domain[6]), a Fourier transform has to be performed. Otherwise (e.g. for the Waveguide Method[7]), the resulting spectrum is processed. In case of a rigorously computed mask spectrum, the "Hopkins" or the "No Hopkins" approach can be applied.[8] Using the Hopkins approximation, only one rigorous computation, typically for a source point on the optical axis, is performed. The diffraction spectra for the other source points are determined by shifting the originally computed spectrum according to the illumination angle of the respective source point. If no Hopkins approximation is selected, the mask diffraction spectra are rigorously computed for several selected illumination source points. The number of rigorous computations is specified by the number of "No-Hopkins" orders. The diffraction spectra of the remaining intermediate source points are obtained by interpolation. In both cases, a fully vectorial description of the mask spectrum is employed (1), taking into account the polarization of the individual source points. In the next step, the mask diffraction spectrum is transformed from the mask plane to the pupil entrance plane and onward into the pupil (2). The pupil transfer function is applied to the spectrum (3). For that, the pupil transfer function is computed at the spatial frequencies of the mask diffraction spectrum. This function accounts for properties like the NA, defocus, filters or polarizers, but also complex characteristics like Jones data or aberrations defined by Zernike polynomials (4). After application of the pupil function, the spectrum is transformed according to the pupil's exit plane (5), after which an inverse Fourier transform yields the complex fields and so the intensities in the image plane (6). These steps are repeated for all source points. The superposition of the images resulting from the individual points (7) leads to the final image.

For efficiency reasons, the kernel of this module has been implemented in the programming language C++, using the well-established expression template technique for the representation of arrays such as vectors and matrices, utilizing the Blitz++ library for this purpose.[9] The expression template pattern uses the fact that C++ templates are Turing complete, that is, template expressions themselves are computationally as powerful as traditional programming languages. The evaluation of expressions is performed during program compilation, thus significantly improving the run-time behavior of a program. In order to guarantee a high degree of flexibility, the user-interface of the imaging module is implemented in the modern scripting language Python. For example, to alter or extend parts of the imaging kernel, the user can extend the corresponding class and have the kernel use this extension instead of the original version of the class. Furthermore, any public data in the imaging kernel can be accessed from Python, for read or manipulation access.

Numerous benchmark tests demonstrate the significant improvement of computation times compared with a standard Abbe approach.[10]

3. DOUBLE EXPOSURE SUPERPOSITION OPTIONS FOR BASIC LAYOUTS

In this section, a simulation study on different superposition techniques for double exposure is discussed. All examinations are restricted to aerial images and a simple threshold model which replaces full resist evaluations. In the first sub-section, superposition models are derived from well-established photoresist models. Different basic layouts are then studied using these superposition approaches.

3.1 Superposition Models

The exposure and bleaching processes in photosensitive materials can be described by the Dill model that can be stated by the following coupled PDEs:

$$\frac{\partial I(z,t)}{\partial z} = -I(z,t)\left(AM(z,t) + B\right) \quad (1)$$

$$\frac{\partial M(z,t)}{\partial t} = -I(z,t)M(z,t)C, \quad (2)$$

where

z	is the position in the material,
t	is the exposure time,
I	is the light intensity,
M	is the normalized concentration of the chemical species and
A, B, C	are (measurable) constants of material properties.

For the purpose of this study we will neglect the impact of the incident light on the optical properties (refractive index n and extinction k) of the photoresist. In order to model different double exposure resist behaviors, we introduce a function r, which describes the response of the resist in dependence of the intensities of the first and second exposure:

$$\frac{\partial M(z,t)}{\partial t} = -r\left(I(z,t)\right) M(z,t) C \tag{3}$$

With this model simplification different superpositions of the intensities of the first and second exposures (I_1, I_2) can be described. A linear superposition is achieved by:

$$r : (I_1, I_2) \mapsto (I_1 + I_2)/2. \tag{4}$$

For a non-resonant two-photon absorption photoresist, a simple quadratic version of this response function can be adopted:

$$r : (I_1, I_2) \mapsto (I_1^2 + I_2^2)/2 \tag{5}$$

In the case of a reversible contrast enhancement layer (RCEL), the response of the photoresist to the incident light is governed by the non-linear transmission of light through the bleachable contrast enhancement layer. Oldham formulated an analytical model to express the received dose (D_R) below the RCEL as a function of the incident dose (D_I) on top of the RCEL.[11,12]

$$e^A = \frac{e^{D_I} - 1}{e^{D_R} - 1} \quad \Rightarrow \quad D_R = \log\left(e^{D_I} + e^A - 1\right) - A \quad \Rightarrow \quad \hat{r}(D_I) = \log\left(e^{D_I} + e^A - 1\right) - A \tag{6}$$

where D_I denotes the incident dose, D_R is the received dose and A is a bleaching parameter of the CEL. Thus, in the regime of a reversible contrast enhancement layer (RCEL), the exposure superposition can be stated as:

$$r : (I_1, I_2) \mapsto \frac{\hat{r}(D_{I_1}) + \hat{r}(D_{I_2}) - 2R_{\min}}{2\hat{r}(2D)} \frac{1}{R_{\max} - R_{\min}}, \tag{7}$$

where
- $\hat{r}$ is the response function as defined in (6),
- D is the exposure dose,
- D_{I_1}, D_{I_2} are the incident doses of the individual exposures, with $D_{I_n} := DI_n$,
- $R_{\max}$ is the maximum received dose for a single exposure, with $R_{\max} := \hat{r}(D)/\hat{r}(2D)$,
- $R_{\min}$ is the minimum received dose, for simplicity $R_{\min} := 0$ throughout this work.

Here, the minimum and the maximum received doses ($R_{\min}$ and $R_{\max}$, respectively) are used in order to normalize the resist response to a range between 0.0 and 1.0. This model is applicable only to thin photoresists as it does not account for diffraction. It has been shown, that for photoresists with a thickness of 22 nm and more, the modulation is significantly degraded.[13]

As another alternative, one can model a threshold behavior of the resist: A chemical modification of the resist occurs only above a certain threshold. At present, no photoresist with such a non-linear behavior is available. In order to examine the performance of a such a cooked-up resist, a model by Weiß et al., originally established to describe the development of chemically amplified resists in dependence of the photo-generated acid concentration,[14] has been adopted:

$$\hat{r} : I \mapsto R_{\min} + \frac{1}{2}\left(R_{\max} \tanh\left(\frac{(I - I_0)\ RS}{R_{\max}}\right) \sqrt{\left(R_{\max} \tanh\left(\frac{(I - I_0)\, RS}{R_{\max}}\right)\right)^2 + \rho_1^2}\right), \tag{8}$$

where
- $R_{\max}$ is the maximum received dose,
- $R_{\min}$ is the minimum received dose,
- I_0 is the threshold intensity,
- RS is the slope of the received dose curve and
- ρ_1 is the curvature near the threshold intensity.

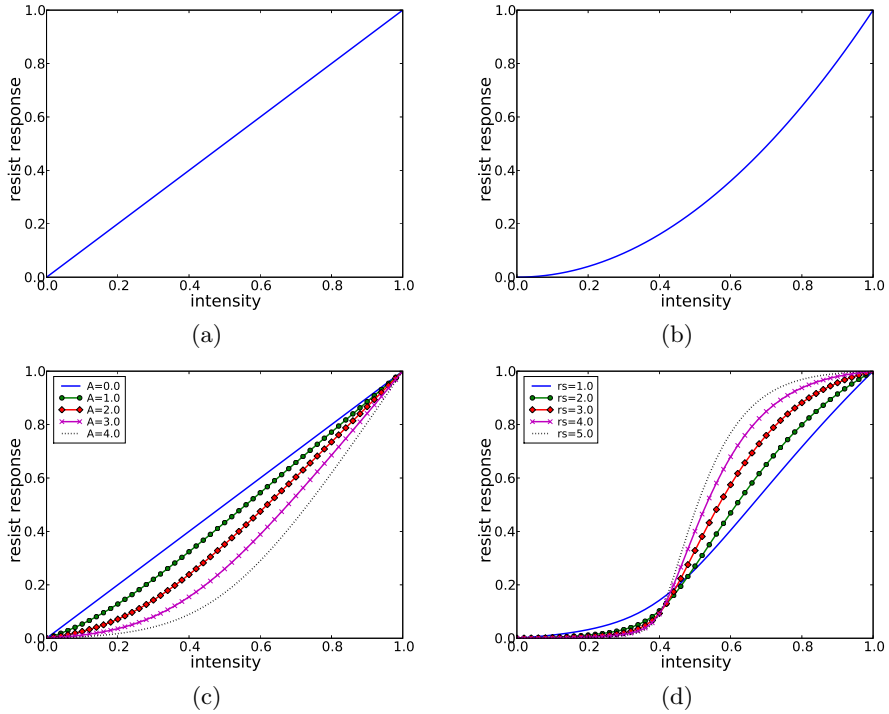

Figure 2. Photoresist response functions: (a) linear superposition, (b) two-photon resist, (c) reversible contrast enhancement layer and (d) threshold model.

Thus, the double exposure response function is given by:

$$r : (I_1, I_2) \mapsto \frac{\hat{r}\,(I_1) + \hat{r}\,(I_2) - 2\,\hat{r}\,(I_{\min})}{2\,(\hat{r}\,(I_{\max}) - \hat{r}\,(I_{\min}))} \tag{9}$$

Figure 2 shows typical photoresist response graphs for different types of superposition. Standard resists can be described by a linear superposition (a). The RCEL and threshold response curves are plotted for different parameter settings. The parameter A for the bleachable absorption in the RCEL model (c) is used to adjust the divergence from the linear response (which is obtained if $A = 0$). The slope parameter RS of the threshold model (d) is used to define the slope of the resist response close to a given threshold intensity.

3.2 Pitch Division for Dense Lines

All simulations have been conducted for water immersion lithography. An NA of 1.35, which is the practical limit in the regime of water immersion, is employed. For simplicity, binary masks and the Kirchhoff near field diffraction formulation were assumed, however, using a full vectorial imaging model. Instead of a rigorous resist model, aerial images and process windows were evaluated using a threshold model. Other, more realistic model options such as alternating phase-shifting masks, rigorous Maxwell solvers for the near field of the masks or a full resist model can be applied in a straightforward manner.

In a first simulation experiment, double exposure was applied to a dense line/space pattern in order to obtain smaller pitches, pushing the k_1 factor below its theoretical limit of 0.25 for dense features. The mask in this example was assumed to be binary. A line/space bias was introduced: $\ell = p/2 \cdot b$, where ℓ is the line width, p is the pitch and b is the bias factor, optimized to provide the maximum dose latitude for the given target. As illumination, a polarized dipole was used. The position of the poles was determined such that a symmetric interference of zeroth and first order was obtained. Consequently, the position of the poles depends on the pitch.

Figure 3 shows a comparison of both a single exposure and a double exposure process. A linear superposition was applied for the aerial images. The single exposure was conducted for 60 nm dense lines (120 nm pitch): Both an excellent contrast and a large depth of focus (DoF) were achieved. In the double exposure case, each exposure was conducted with a doubled pitch of 240 nm. The deviation of threshold-to-size from the isofocal threshold

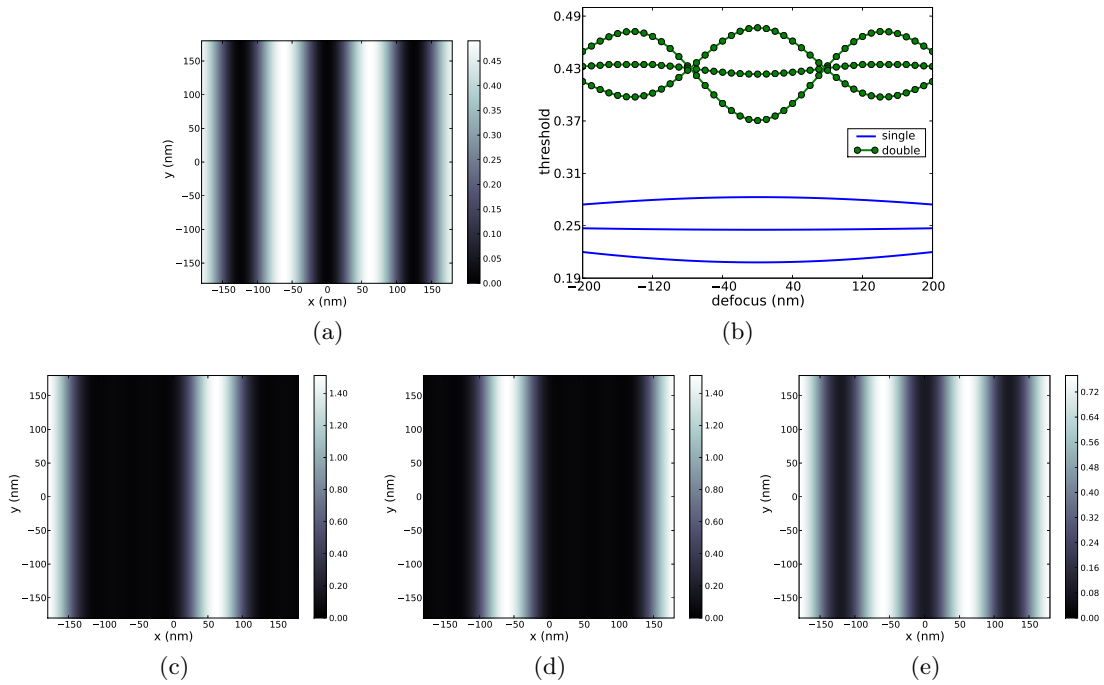

Figure 3. Simulation results for dense line/space pattern. Aerial images for (a) single exposure and (e) double exposure, with a linear superposition of the individual exposures (c) and (d); (b) process windows for both single and double exposure. The double exposure process window exhibits three lobes. This behavior can be attributed to a polarity inversion originating from contributions of higher diffraction orders.

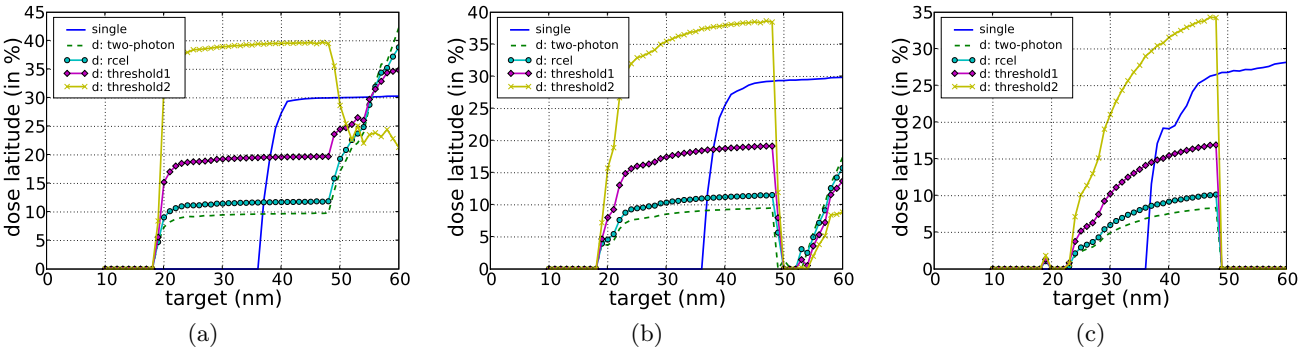

Figure 4. Comparison of single exposure and different double exposure superposition techniques in terms of dose latitude as a function of target size at (a) 50, (b) 100, (c) 200 nm depth of focus.

and the contribution of higher diffraction orders, compared with the single exposure case, degrades the DoF and the contrast of the aerial image. On the other hand, the same property, the presence of higher diffraction orders for a given target pitch, enables the imaging of smaller line/space patterns with smaller pitches and line widths. This, however, requires elaborate superpositions techniques for the single exposure steps.

Figure 4 compares different exposure superposition techniques for different depths of focus. For the single exposure, no dose latitude is maintained for targets of 36 nm (= 0.25λ/NA) and below. While the slope is very steep for small depths of focus (e.g. 50 nm), larger DoFs result in a slightly more gradual increase of dose latitude. All non-linear superposition techniques shift the dose latitude fall-off to 18 nm, thus yielding a significant resolution improvement. Similarly to the single exposure case, with increasing DoFs, the gradient of target vs. dose latitude decreases. The dose latitude strongly depends on the superposition option: two-photon and RCEL show a dose latitude below the one achieved with single exposure. The threshold model with a slope parameter RS of 1.4 (*"threshold1"*) still shows a slightly smaller dose latitude, whereas the same model with $RS = 3.0$ (*"threshold2"*) has a dose latitude above the single exposure one.

3.3 Formation of Contact Holes by Exposure of Orthogonal Line Patterns

In this second example, two orthogonal line/space patterns were successively imaged to form a contact hole pattern with a larger process window than achievable with a single exposure step. Figure 5 illustrates this idea which was first published by Korobko et al.[1] A practical realization utilizing a resist freezing process was proposed by Nakamura et al.[2,15]

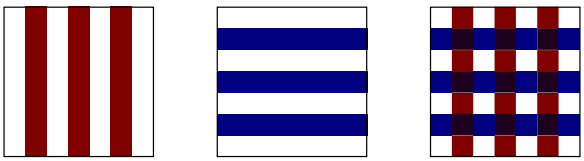

Figure 5. Formation of a dense array of contact holes (c) by subsequent exposures of two orthogonal lines/spaces patterns (a) and (b).

First simulations were performed for dark field mask, using a (hypothetical) positive resist. Figure 6 depicts aerial images for both a single exposure and the double exposure technique using two orthogonal line/space patterns. For the single exposure, a target of 60 nm and a pitch of 120 nm in both directions was aimed at. Again, a feature/pitch bias was introduced: $s = p/2 \cdot b$, where s is the feature size, p is the pitch and b is the bias factor. A x-y-polarized CQuad served as illumination source. The position of the poles was determined (for each pitch individually) such that zeroth and first diffraction orders symmetrically interfere.

Double exposures were conducted with a line/space mask for a 60 nm target and 120 nm pitch. The same bias correction as for the pitch division example was performed. In addition, a similar illumination set-up, using dipoles with a pitch-dependent position that allows for a symmetric interference of zeroth and first orders, was chosen. However, a different orientation both for the mask and for the dipoles was applied to the first and the second exposure (see Figure 5). For the given pitch (60 nm) and linear polarization both resulting images have the same contrast; the process windows differ only by a scaling factor along the threshold axis; this difference can be explained in terms of the diffraction efficiencies of the arrays of contacts and lines/spaces.

Figure 7 shows simulated dose latitudes for various DoF. For all options, a dose latitude fall-off at 36 nm (0.25λ/NA) can be observed. While a small DoF (50 nm) shows a steep gradient at 36 nm, larger depths-of-focus result in more gradual dose latitude characteristics. The same performance is obtained with single exposure and linear double exposure for pitches up to 76 nm. The contribution of (different) higher diffraction orders results in an option-dependent behavior for larger pitches. Although all non-linear superpositions improve the dose latitude, the threshold model shows the most significant improvement. Like in the previous example, two different threshold slope values ($RS = 1.4$ and $RS = 3.0$) have been evaluated, the latter leading to the largest dose latitude.

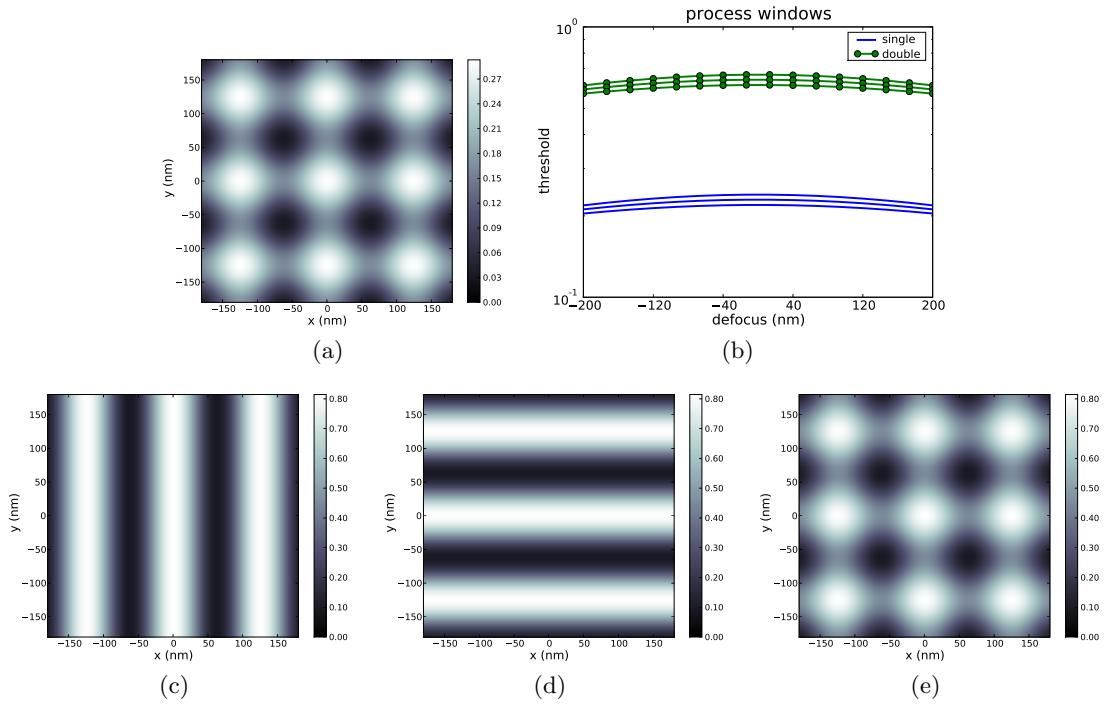

Figure 6. Simulation results for a contact hole array with a dark field mask. Aerial images for (a) single exposure and (e) double exposure, for which a linear superposition of the subsequent exposures of orthogonal line/space patterns (c) and (d) is performed; (b) process windows for both single and double exposure. In order to account for different scaling factors for the doses of single and double exposure, the dose axis has a logarithmic scale.

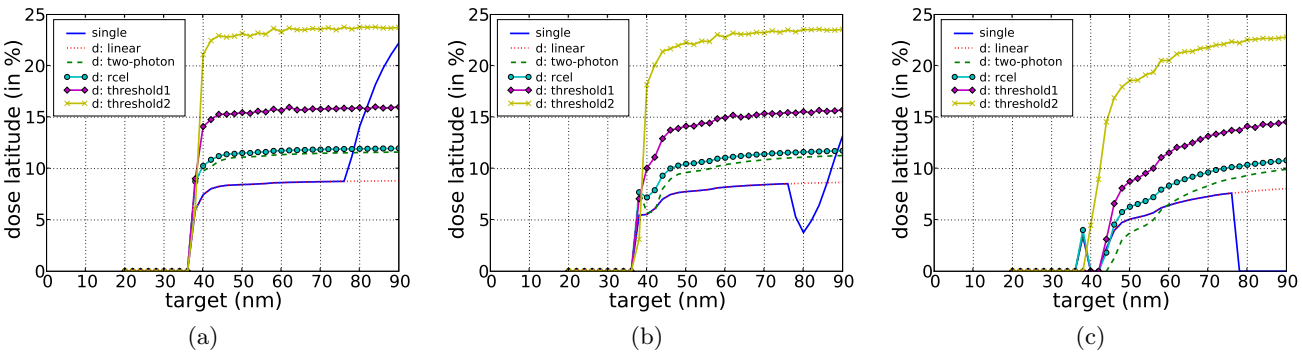

Figure 7. Comparison of single exposure and different double exposure superposition techniques in terms of dose latitude as a function of target size at (a) 50, (b) 100, (c) 200 nm depth of focus.

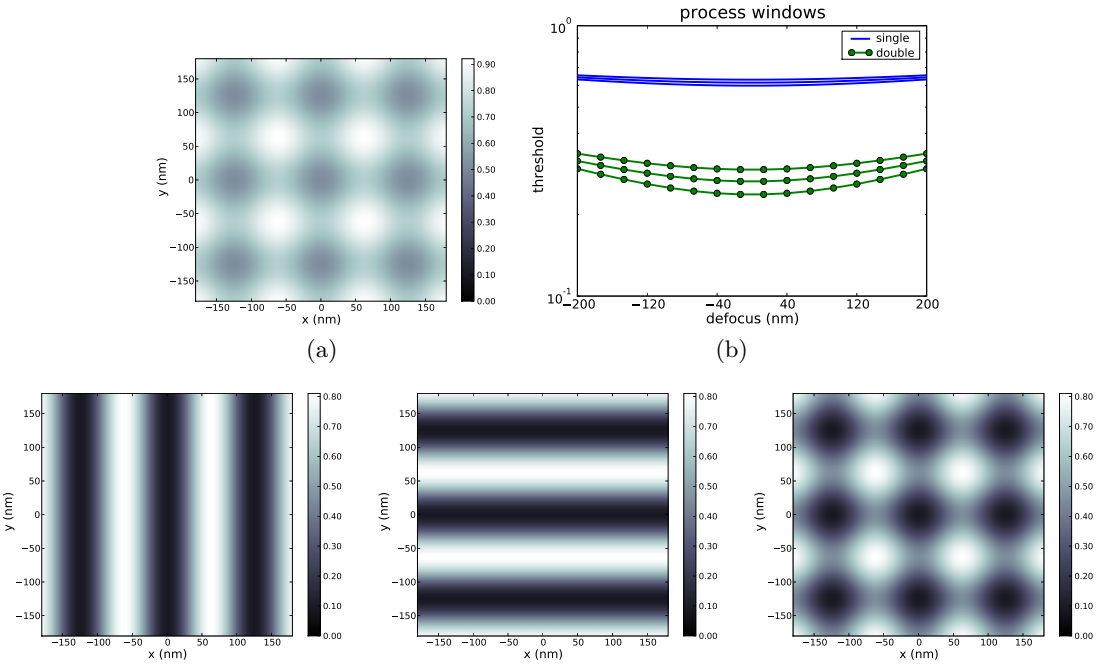

Figure 8. Simulation results for a contact hole array with a bright field mask. Aerial images for (a) single exposure and (e) double exposure, for which a linear superposition of the subsequent exposures of orthogonal line/space patterns (c) and (d) is performed; (b) process windows for both single and double exposure. The different dose scaling factors are taken into account by using a logarithmic scale on the dose axis.

In a similar fashion, contact holes can also be achieved using a bright field mask, and hence dark features. This approach, however, implies the obstacle of a negative resist, which is not yet usable in manufacturing. The same pitch, target and illumination settings as in the former example, that made use of a dark field mask, were applied. But in this example, even the linear double exposure option provides a significantly higher contrast than the single exposure, as can be seen in Figure 8. Moreover, any double exposure technique shows a distinct process window enlargement. The corresponding dose latitude plots are pictured in Figure 9. All double exposure options, even the linear superposition, exhibit larger dose latitudes than the single exposure process. Non-linear superpositions, especially the threshold options, lead to a very robust imaging performance, allowing contact arrays with a target dimension of 40 nm times 40 nm to be printed even at 300 nm DoF. It is noteworthy that the double exposure approach require higher exposure doses. This drawback is even more pronounced in the scope of non-linear superpositions.

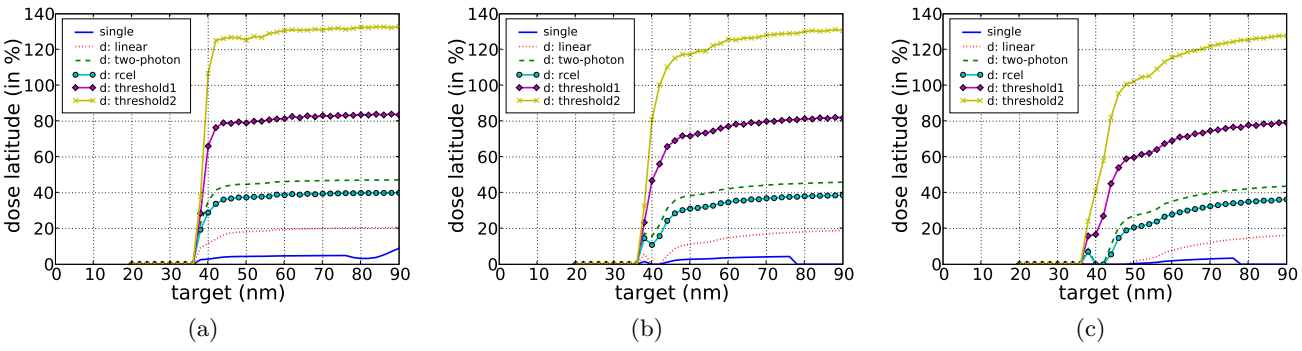

Figure 9. Comparison of single exposure and different double exposure superposition techniques in terms of dose latitude as a function of target size at (a) 100, (b) 200, (c) 300 nm depth of focus.

4. APPLICATION OF TWO-PHOTON AND DOUBLE PATTERN SIMULATION TO INTERFERENCE-ASSISTED LITHOGRAPHY

Elsewhere in these series of conferences, we present interference-assisted lithography (IAL) as a promising and cost-effective solution for extending lithography to the 22 nm technology node and beyond.[16] As shown in Figure 10, IAL achieves a final pattern by combining a maskless interference exposure with a trim or blocking exposure with projection lithography of a mask pattern.

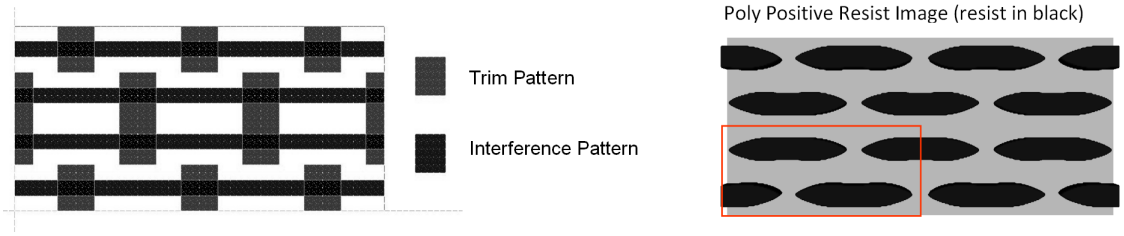

(a) (b)

Figure 10. (a) Mask pattern and (b) final resist pattern for the SRAM poly layer. The box outlines the unit cell.[16]

This method allows maskless exposure at numerical apertures greater than 1.35 using wavelengths at and below 193 nm (even EUV). It does so in a fashion that maintains symmetrically placed transistors over source and drain, a failure point of other double imaging processes, yet at the same time, due to its very high image contrast, with a minimum of image contrast related line-edge-roughness.[17] IAL is a variant of methods proposed by Fritze et al. at Lincoln Labs that, as possible, uses binary and phase-shifted assist features to improve the imaging of the trim or blocking exposure which without the assists typically has marginal image quality.[3,18] Here, however, we do not use assist features to enhance the resist imaging contrast so as to better see the effects of introducing non-linear imaging into the system.

In this work, we have examined imaging the 90 nm pitch, 25 nm transistor poly-layer of a six transistor SRAM cell[4,16] using a single exposure of a 6% attenuated phase shift mask for reference, and IAL with an interference exposure to produce a 90 nm pitch pattern combined with a chrome mask blocking exposure to define the transistors. As Figure 10 shows, there is considerable taper near the end caps whose elimination or reduction could greatly improve both the performance and the predictability of the device. We have simulated linear and non-linear imaging processes. Specifically, we have examined single-photon and two-photon resist processes both in an exposure only process (single or the IAL double) and using IAL in a double patterning process where one pattern is imaged, transferred into a hard mask, recoated with resist, and the second pattern is made and transferred. In this current work, the impact of substrate topography or etch is not taken into account.

4.1 Focus-Exposure Process Window Simulations

For lithography simulation, Dr.LiTHO (version 0.12.rc3) with full vector models on thin mask and high contrast positive 50 nm resist model parameters for simple acid diffusion and 10% quencher to photo-acid-generator loading is employed. Because of the type of diffusion model used, we chose a short post-exposure-bake time of 10 seconds and a develop time of 40 seconds. These process times were selected after running a full factorial of the poly layer for 90 nm-pitch SRAM and choosing the maximum process latitude for the reference single exposure and binary blocking exposure processes.

The 1D regular-pitch SRAM bitcell used for the lithography simulation was designed on 30×12 grids with 15 nm per grid and has the same pitch for all layers except diffusion layer, as shown in Figure 11. A simple OPC correction using biasing is applied. We have used an ASML-type cross-quadrupole (XQuad) shape that is 0.25 sigma wide, centered at 0.65 sigma and has a blade angle of 20 deg. with x-y azimuthal-like polarization for the trim exposure with NA = 1.2 to trim the 90 nm pitch interference pattern. The interference lithography (IL) was emulated by imaging an alternating phase-shift mask with an on-axis coherent source. We have used a positive-tone resist for the poly layer. The single exposure process was realized with a 6% attenuated 180 deg. phase

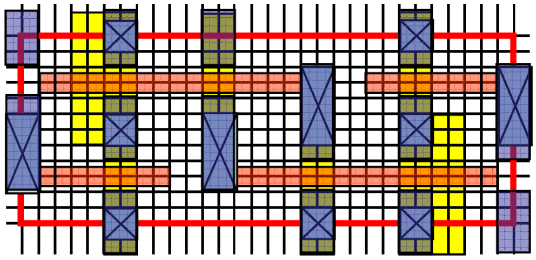

Figure 11. Layout of the 30 × 12 grids 1D regular pitch SRAM bitcell used for the lithography simulation.[3,4]

mask with a numerical aperture of 1.2 using an ASML-type cross-quad illuminator shape with x-y azimuthal-like polarization that was optimized for the x and y oriented pitches using $\sigma_{\text{x-center}} = 0.27$ and $\sigma_{\text{y-center}} = 0.89$ with a $\sigma_{\text{width}} = 0.15$. We have implemented the two-photon simulations by squaring the image intensity in resist for each exposure before completing PEB and development. Please note that no correction in the Dill C parameter was applied though it would be greatly reduced in a true two-photon or, the preferred, aggregate two-photon process.

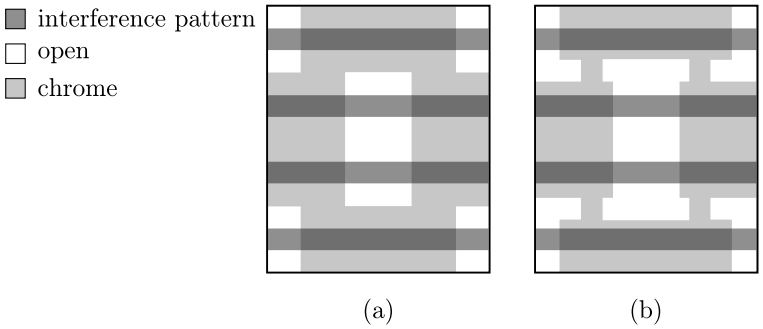

Figure 12. Because there is no highly exposed resist near the blocking exposure, double patterning provides the opportunity to add additional OPC structures in the form of hammer heads that provide a more ideal shape after final processing. The mask used for "IAL" and "double patterning (DP) with blocking" is shown on the left. The mask used for "double patterning with hammer head" is shown on the right.

We have simulated double patterning for each single-photon or two-photon exposure by simulating both the interference pattern and blocking patterns through PEB. We have then selected the maximum acid concentration between the two exposures at each simulation node and developed the result. As illustrated in Figure 12, because there was no highly exposed resist near the blocking exposure to distort the adjacent lines, double patterning provides the opportunity to add additional OPC structures in the form of hammer heads that provided a more ideal shape after final processing.

Typically, lithography process studies only aim at comparing critical dimension (CD) tolerance for ±10% CD control and thus neglect actual requirements for a functioning transistor. So does this study. However, a more global view on the problem will be provided. Referring to Figure 13, as poly traverses the diffusion area nearest the end, the CD_{taper}, is typically narrower than the "inner" poly, the CD_{inner}, at the other edge of the diffusion area. For this work, we have allowed the CD_{inner} to range from 29 nm to 35 nm, and we have sought to maximize the CD_{taper} without scumming the resist between the opposing poly ends by setting the CD of the gap between these ends, the CD_{gap}, to be $45\,\text{nm} \geq \text{CD}_{\text{gap}} \geq 10\,\text{nm}$ while at the same time maximizing the ratio of the CD_{taper} to CD_{inner}. With these criteria for the boundaries, we have examined the imaging potential of IAL compared with the single exposure imaging process.

CD	min. (nm)	max. (nm)
gap	10	45
inner	22	27
middle	22.5	27.5
taper	10	35

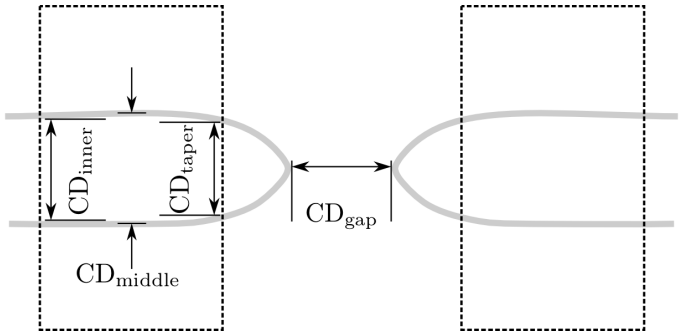

Figure 13. Diagram of critical dimension boundary conditions. Whichever CD boundary is first encountered constrains the overall process window. The analysis in Figure 14 ignores CD_{inner}, which is considered in the text.

4.2 Focus-Exposure Process Window Simulation Results

Figure 14 shows the exposure latitude versus depth of focus for the various processes evaluated; it also includes a top-down perspective image of the resist for selected processes. Linear and non-linear resists in double patterning were identical, so only one is shown in the figure. The legend is listed from largest exposure latitude to the smallest at 0.100 µm depth of focus with the single exposure/two-photon being approximately equivalent to the double pattern using the regular blocking mask.

Table 1. Exposure latitude analysis for the various processes: percent at 0.1 µm DoF (second column), relative to the single exposure process (third column), two- to single-photon ratio (fourth column) and relative to the respective IAL process (fifth column).

Process	Exposure latitude (%) at 0.1 µm DoF	Relative to:		
		Single Exposure	2:1 photon	DP:IAL
Single-Photon				
IAL	12.5	3.4		*(reference)*
DB Hammer Head	9.1	2.5		0.73
DB Blocking	7.8	2.1		0.62
Single Exposure	3.7	*(reference)*		
Two-Photon				
IAL	26.4	7.2	2.1	*(reference)*
DP Hammer Head	21.6	5.9	2.4	0.82
DP Blocking	20.1	5.5	2.6	0.76
Single Exposure	9.2	2.5	2.5	

Table 1 shows a % exposure latitude process window ratio analysis of the various processes relative to the single exposure process in the first column, relative to the single-photon case in the second column, and relative to the respective IAL process in the final column. These results show that IAL variants exhibit the largest processing capability and that the two-photon processes are more than two to two and half times better than their single-photon, conventional resist analogs. Introducing resist response non-linearity also improved the transistor shape of the single and double exposure processes. Thus allowing in the case of IAL to change the CD_{taper} from 10 nm to 23 nm, resulting in essentially the same process capability of the 10 nm limited linear resist IAL process whose maximum simulated CD_{taper} is reported to be 17 nm, using the same models as this study.[16] The IAL-modified double patterning's process windows are smaller than the ones of IAL when using the restricted limits of 10 nm for both the CD_{taper} and CD_{gap}, but larger when CD_{gap} is set to 23 nm. With the same limits, there is also a 7.8 to 9.1 times process window improvement compared to the single exposure process for the conventional resist. However, when the process tolerance is set to a poly width tolerance of 23 to 27 nm at all three active intersection locations (CD_{taper} , CD_{middle} and CD_{inner}), it is by far the best choice for

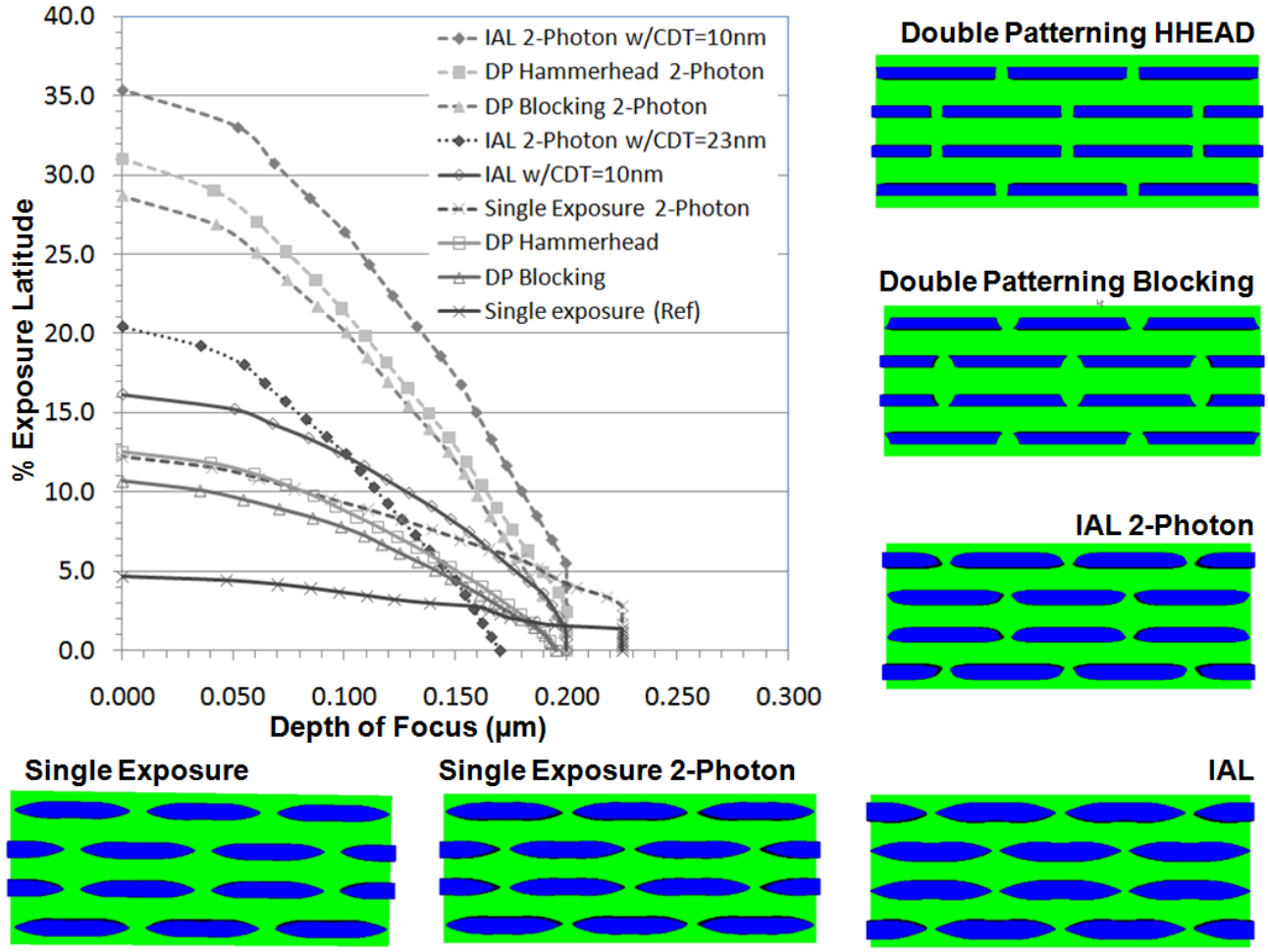

Figure 14. Focus-exposure summary plot combined with select best dose and focus top-down perspective resist images (black). Excluding the double pattern (DP) results, the size of the process windows were constrained by CD_{taper} (CDT); double pattern was constrained by CD_{gap}. Solid curves and open markers represent the conventional resist exposure, dashed line curves and solid markers represent two-photon resist processes and the dotted line represents the two-photon IAL process with CD_{taper} set to 23 nm.

imaging the 90 nm pitch poly-layer – with the IAL double patterning of the hammer head mask being the best, due to the squareness of the transistors' corners.

5. CONCLUSIONS

In this paper, we have presented numerous simulation experiments aimed at exploring different double exposure and double patterning scenarios, for which a briefly introduced new imaging tool in combination with a flexible simulation environment has proven to be of considerable advantage. The lithographic performance of several options of optical non-linearities such as two-photon absorption, reversible contrast enhancement layers and threshold-based responses have been presented and compared. It has been shown that threshold-type optical non-linearities provide a better performance than two-photon processes and a reversible contrast. Very large (unrealistic) resist non-linearities are required to pattern dense lines with $k_1 < 0.25$ by double exposure. Even minor resist non-linearities can provide a strong process improvement for "standard" double exposure techniques such as the creation of contact holes by orthogonal line/space patterns. The selection of the most appropriate double exposure/double patterning option strongly depends on the layout and on the considered target region.

It has also been demonstrated that interference-assisted lithography (IAL) benefits from the use of these non-linear systems. Even "standard" IAL provides a threefold improvement of the process window over single exposure lithography. Using the initial processing CD limits of 10 nm for both taper and gap CD as an arbitrary construct, we have shown that double exposure IAL within a single-photon or two-photon family yields the best imaging potential of the processes considered. However, when all processing limits are considered, the IAL double pattern processes provided the best transistor shape and thus the best overall processing results. Further, it was shown that combining non-linear resists with any of the imaging processes more than doubles the imaging potential of each respective system. While IAL provides some serious but solvable design challenges, its significant potential for achieving 32 nm pitch design rules could be shown.

Acknowledgments

The authors from Fraunhofer IISB would like to thank the European Commission for funding parts of this work in the framework of the European research project "MD3".

The authors from Petersen Advanced Lithography want to acknowledge Zhilong Rao and Rudi Hendel of Applied Materials and Anantha Sethuraman and Vichu Viswanathan of DFMSim for financial support of this work. And they want to acknowledge Chris Mack who got them involved with the IAL project at Applied.

Finally, we dedicate this paper to the late Jeff Byers whose tragic death in November 2008 robbed us of his imagination, his dizzying intellect and, most importantly, his spirit and humanity. And, we acknowledge Jeff's contribution to our evolving thought in non-linear imaging. Thank you Jeff!

REFERENCES

[1] Korobko, Y., Liu, M., Talens, J., and Powers, J., "Resolution limits with 248nm strong phase shifting techniques for contact patterning applications," in [*Proc. SPIE*], **3546**, 594–605 (1998).

[2] Nakamura, H., Onishi, Y., Sato, K., Tanaka, S., Mimitogi, S., Hashimoto, K., and Onoue, S., "Contact hole formation by multiple exposure technique in ultralow k1 lithography," *J. Microlith., Microfab., Microsyst.* **4**(2), 023005 (2005).

[3] Fritze, M., Bloomstein, T. M., Tyrrell, B., Fedynyshyn, T. H., Efremow, Jr., N. N., Hardy, D. E., Cann, S., Lennon, D., Spector, S., Rothschild, M., and Brooker, P., "Hybrid optical maskless lithography: Scaling beyond the 45 nm node," *J. Vac. Sci. Technol. B* **23**(6), 2743–2748 (2005).

[4] Greenway, R. T., Jeong, K., Kahng, A. B., Park, C.-H., and Petersen, J. S., "32nm 1-d regular pitch sram bitcell design for interference-assisted lithography," in [*Proc. SPIE*], **7122**(1), 71221L (2008).

[5] Byers, J., Lee, S., Jen, K., Zimmerman, P., Turro, N., and Willson, C. G., "Double exposure materials: Simulation study of feasibility," *Journal of Photopolymer Science and Technology* **20**(5), 707–717 (2007).

[6] Erdmann, A. and Friedrich, C., "Rigorous diffraction analysis for future mask technology," in [*Proc. SPIE*], **4000**, 684—694 (July 2000).

[7] Evanschitzky, P. and Erdmann, A., "Fast near field simulation of optical and euv masks using the waveguide method," in [*Proc. SPIE*], **6533**, 65530Y (2007).

[8] Erdmann, A., Citarella, G., Evanschitzky, P., Schermer, H., Philipsen, V., and De Bisschop, P., "Validity of the Hopkins approximation in simulations of hyper-NA (NA > 1) line-space structures for an attenuated PSM mask," in [*Proc. SPIE*], **6154**, 167–178 (Apr. 2006).
[9] Veldhuizen, T. L., "Arrays in Blitz++," in [*Proceedings of the 2nd International Scientific Computing in Object-Oriented Parallel Environments (ISCOPE'98)*], *Lecture Notes in Computer Science*, Springer-Verlag (1998).
[10] Evanschitzky, P., Erdmann, A., and Fühner, T., "Extended Abbe approach for fast and accurate lithography imaging simulations," in [*Proceedings of the 25th European Mask and Lithography Conference*], (2009), to be published.
[11] Oldham, W., "The use of contrast enhancement layers to improve the effective contrast of positive resist," *IEEE Transcations on Electron Devices* **34**(2), 247–251 (1987).
[12] Kim, R.-H. and Levinson, H. J., "Application of contrast enhancement layer to 193 nm lithography," *J. Vac. Sci. Technol. B* **25**(6), 2466–2470 (2007).
[13] Erdmann, A., Evanschitzky, P., Fühner, T., Schnattinger, T., Xu, C., and Szmanda, C., "Rigorous electromagnetic field simulation of two-beam interference exposures for the exploration of double patterning and double exposure scenarios," in [*Proc. SPIE*], **6924**, 692452 (2008).
[14] Weiß, M., Binder, H., and Schwalm, R., "Modeling and simulation of chemically amplified duv resist using rhe effective acid concept," *Microelectr. Engineering* **27**(1-4), 405–408 (1995).
[15] Nakamura, H., Omura, M., Yamashita, S., Taniguchi, Y., Abe, J., Tanaka, S., and Inoue, S., "Ultralow k1 oxide contact hole formation and metal filling using resist contact hole pattern by double line and space formation method," *J. Micro/Nanolith.MEMS MOEMS* **7**(4), 043001 (2008).
[16] Greenway, R. T., Hendel, R., Jeong, K., Kahng, A. B., Petersen, J. S., Rao, Z., and Smayling, M. C., "Interference assisted lithography for patterning of 1d gridded design," in [*Proc. SPIE*], **7271** (2009), to be published.
[17] Hinsberg, W., Houle, F. A., Hoffnagle, J., Sanchez, M., Wallraff, G., Morrison, M., and Frank, S., "Deep-ultraviolet interferometric lithography as a tool for assessment of chemically amplified photoresist performance," *J. Vac. Sci. Technol. B* **16**, 3689–3694 (Nov. 1998).
[18] Fritze, M., Tyrrell, B., Fedynyshyn, T., Rothschild, M., and Brooker, P., "High-throughput hybrid optical maskless lithography: all-optical 32-nm node imaging," in [*Proc. SPIE*], **5751**, 1058–1068 (May 2005).